Magnetization reversal within Dzyaloshinskii–Moriya interaction under on-site Coulomb interaction in $BiCrO_3$

Feng Hong-Jian(冯宏剑)†

Department of Physics, Northwest University, Xi'an 710069, *China*

(Received 9 March 2012; revised manuscript received 11 April 2012)

First-principals calculations show that magnetization reversal is accompanied by the opposite sense of rotation of the neighboring oxygen octahedra along the [1 1 1] direction which is called the antiferrodistortive displacement in $BiCrO_3$. The coupling between magnetization and antiferrodistortive distortion is mainly caused by Dzyaloshinskii–Moriya interaction which is driven by the e_g–e_g states antiferromagnetic interaction in Cr-3d. A critical value of on-site Coulomb interaction prohibiting the Dzyaloshinskii–Moriya interaction and thus the magnetization reversal is found to be 1.3 eV.

Keywords: Dzyaloshinskii–Moriya interaction, density of states, $BiCrO_3$

PACS: 71.15.Mb, 75.30.Et, 75.30.GW **DOI:** 10.1088/1674-1056/21/8/087103

1. Introduction

Multiferroics have attracted much interest because magnetic and electronic ordering can coexist in the same phase. Magnetism can correlate with ferroelectricity by direct interaction or indirect structure mediated correlation in multiferroics. The coupling of the two ordering leads to the so-called magnetoelectric effect in which the magnetization can be tuned by the external electric field, and *vice versa*.[1,2] Magnetoelectrics have potential application in information storage and emerging spintronics which makes them a hot spot in multifunctional materials. Perovskite $BiFeO_3$ has long been known to be ferroelectric with a Curie temperature of 1103 K and antiferromagnetic (AFM) with a Néel temperature of 643 K.[3] Magnetic moment of iron ions are arranged antiferromagnetically along the [1 1 1] crystalline direction while they are ferromagnetic (FM) ordering in the (1 1 1) plane which is called the G-type AFM order. The G-type AFM order of Fe magnetic moments exhibits a canting caused by the antisymmetric Dzyaloshinskii–Moriya interaction (DMI) under rhombohedral $R3c$ space group.[4,5] In addition to the ferroelectric displacement of the Bi site driven by a Bi-6s stereochemically active lone pair induced by mixing between the $(ns)^2$ ground state and a low-lying $(ns)^1(np)^1$ excited state, an antiferrodistortive (AFD) distortion (the alternating sense of rotation of the oxygen octahedra along the [1 1 1] direction) can be observed simultaneously.[6,7] In our preceding paper, we suggest that AFD distortion couples with the weak ferromagnetism due to the DMI. Magnetization reversal can be tuned by AFD distortion reversal with an active DMI. Meanwhile the DMI is inversely proportional to the on-site Coulomb interaction (U).[8−10] Based on the weak ferromagnetism in $BiFeO_3$, Spaldin and coworkers have predicted the novel multiferroic, Bi_2FeCrO_6, which has large polarization and magnetization, and prepared it soon after.[11,12] In the new system, Fe is replaced by Cr periodically along the [1 1 1] direction, reducing the space group to $R3$. In addition they systematically investigated the electronic properties of perovskite $BiFeO_3$, $BiCrO_3$, and Bi_2FeCrO_6.[13] It is rational to study the magnetism of $BiCrO_3$ rather than Bi_2FeCrO_6 due to the simple DMI in it. Moreover it paves the way for the further exploration of the complicated DMI. Does AFD distortion couple with magnetism in $BiCrO_3$? Is the magnetization reversal identical to that in $BiFeO_3$? In this paper we will answer the above-mentioned questions and provide the magnetic and electronic properties in $BiCrO_3$, using first-principles calculations.

This paper is organized as follows: In Section 2,

†Corresponding author. E-mail: fenghongjian@gmail.com

© 2012 Chinese Physical Society and IOP Publishing Ltd

we present the computational details. In Section 3 we report the calculated results and discussions. In Section 4, a summary is given.

2. Computational details

We have performed the local spin density approximation (LSDA) and the density functional theory (DFT) calculation using the ABINIT package.[14,15] The ion–electron interaction was modeled by the projector augmented wave (PAW) potentials[16,17] with a uniform energy cutoff ($E_{\rm cut}$) of 500 eV. Bi 5d, 6s, and 6p electrons, Cr 4s, 4p, and 3d electrons, and O 2s and 2p electrons were considered as valence states. Two partial waves per l quantum number were used. The cutoff radii for the partial waves for Bi, Cr, and O were 2.5, 2.3, 1.1 a.u. (atomic unit), respectively. $9\times9\times9$ Monkhorst–Pack sampling of the Brillouin zone was used for all calculations. The coarse plane wave FFT grid is set with all wave vectors up to $3/2G_{\rm cut}$ (normal grid) and $2G_{\rm cut}$ (denser grid) being included, respectively. We use a different FFT grid to test the energy and magnetization. $G_{\rm cut}$ is related to $E_{\rm cut}$ by

$$\frac{\hbar^2}{2m_e}|G_{\rm cut}|^2 = E_{\rm cut}. \tag{1}$$

We calculated the magnetization and electronic properties within the LSDA + U method where the strong Coulomb repulsion between localized d states has been considered by adding a Hubbard-like term to the effective potential.[18−23] The effective Hubbard parameter (U'), the difference between the Hubbard parameter U and the exchange interaction J ($U-J$), was changing from 0 to 5 eV. We fix J to be 1 eV for different U' in that the magnetization is independent of J.[8,10] We have introduced the noncollinear spin configuration to construct the G-type AFM order, taking into account the spin–orbital (SO) interaction. Two rotational vectors, $\boldsymbol{R}_{\rm in}$ (inward AFD state) and $\boldsymbol{R}_{\rm out}$ (outward AFD state), corresponding to opposite AFD distortions are the same as those in Refs. [8] and [10].

3. Results and discussion

The lattice parameters are introduced as in Ref. [13]. The lattice structures to different rotational vectors are given in Table 1. Rotational vectors for neighboring oxygen octahedra are pointing inward according to the right-hand role in $\boldsymbol{R}_{\rm in}$ while outward in $\boldsymbol{R}_{\rm out}$.

Table 1. Lattice constant a, rhombohedral angle α, volume V, and Wyckoff parameters for $BiCrO_3$, $BiCrO_3$-$\boldsymbol{R}_{\rm in}$, and $BiCrO_3$-$\boldsymbol{R}_{\rm out}$, respectively. The Wyckoff positions $1a(x,x,x)$ for the cations and $3b(x,y,z)$ for the anions.

		$BiCrO_3$	$BiCrO_3$-$\boldsymbol{R}_{\rm in}$	$BiCrO_3$-$\boldsymbol{R}_{\rm out}$
a/Å		5.43	5.43	5.43
α/(∘)		60.37	60.37	60.37
V/Å^3		114.16	114.16	114.16
Bi	x	0.000	0.000	0.000
Cr	x	0.228	0.228	0.228
O	x	0.546	0.493	0.602
	y	0.952	0.961	0.933
	z	0.407	0.451	0.370

In Table 2, we present the net magnetization per unit cell with respect to $\boldsymbol{R}_{\rm in}$ and $\boldsymbol{R}_{\rm out}$, using a normal FFT grid for different U'. Then we increase the grid structure to a denser one to check whether the grid number has an effect on the results and we report the results in Table 3. From Table 2, it is obvious that the y component magnetization is reversed, leading to the total magnetization reversal, when AFD distortions are alternating as U' is under 1.3 eV. While the y component magnetization remains the same sign as U', it is exceeding 1.3 eV. For the sake of clarity, we report that the variation of AFM vectors as U' ranges from 0 eV to 5 eV in Fig. 1. A significant anomaly for y component magnetization can be found at 1.3 eV. This conforms that the critical value prohibiting the magnetization reversal is 1.3 eV. This critical value of U' is smaller than that for $BiFeO_3$ and Bi_2FeMnO_6. For all of these perovskite multiferroics, the canting of magnetization away from x direction is due to DMI.[8,10] Moreover the canted magnetization lies in the xy plane in that the magnetic ions are arranged in the z direction confined by the $R3c$ space group symmetry. Hereby, the net magnetization mainly comes from the y component when DMI is active.

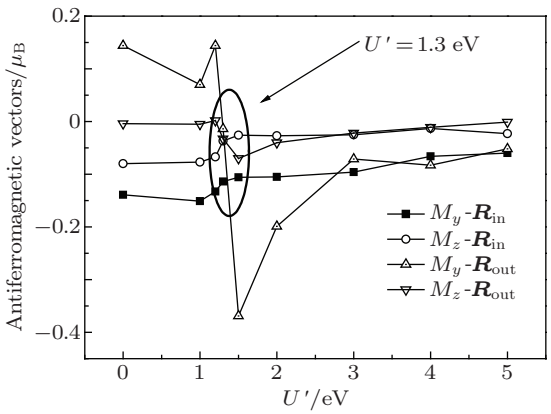


Fig. 1. Relationship between AFM vectors and the effective Hubbard parameter U'.

Table 2. Magnetization per unit cell with respect to different values of U' using a normal FFT grid.

U'/eV	0		1		1.2		1.3		1.5	
	$\boldsymbol{R}_{\rm in}$	$\boldsymbol{R}_{\rm out}$	$\boldsymbol{R}_{\rm in}$	$\boldsymbol{R}_{\rm out}$	$\boldsymbol{R}_{\rm in}$	$\boldsymbol{R}_{\rm out}$	$\boldsymbol{R}_{\rm in}$	$\boldsymbol{R}_{\rm out}$	$\boldsymbol{R}_{\rm in}$	$\boldsymbol{R}_{\rm out}$
$M_x/\mu_{\rm B}$	0.000	0.000	0.000	0.000	0.000	0.000	0.000	0.000	0.000	0.000
$M_y/\mu_{\rm B}$	−0.139	0.144	−0.151	0.070	−0.133	0.144	−0.114	−0.139	−0.106	−0.369
$M_z/\mu_{\rm B}$	−0.080	−0.004	−0.077	−0.005	−0.067	0.002	−0.037	−0.033	−0.026	−0.070
U'/eV	2		3		4		5			
	$\boldsymbol{R}_{\rm in}$	$\boldsymbol{R}_{\rm out}$	$\boldsymbol{R}_{\rm in}$	$\boldsymbol{R}_{\rm out}$	$\boldsymbol{R}_{\rm in}$	$\boldsymbol{R}_{\rm out}$	$\boldsymbol{R}_{\rm in}$	$\boldsymbol{R}_{\rm out}$		
$M_x/\mu_{\rm B}$	0.000	0.000	0.000	0.000	0.000	0.000	0.000	0.000		
$M_y/\mu_{\rm B}$	−0.105	−0.199	−0.096	−0.071	−0.066	−0.083	−0.060	−0.052		
$M_z/\mu_{\rm B}$	−0.027	−0.040	−0.025	−0.022	−0.013	−0.011	−0.023	−0.001		

Table 3. Magnetization per unit cell with respect to different values of U' using a denser FFT grid.

U'/eV	0		1		1.2		1.3		1.5	
	$\boldsymbol{R}_{\rm in}$	$\boldsymbol{R}_{\rm out}$	$\boldsymbol{R}_{\rm in}$	$\boldsymbol{R}_{\rm out}$	$\boldsymbol{R}_{\rm in}$	$\boldsymbol{R}_{\rm out}$	$\boldsymbol{R}_{\rm in}$	$\boldsymbol{R}_{\rm out}$	$\boldsymbol{R}_{\rm in}$	$\boldsymbol{R}_{\rm out}$
$M_x/\mu_{\rm B}$	0.000	0.000	0.000	0.000	0.000	0.000	0.000	0.000	0.000	0.000
$M_y/\mu_{\rm B}$	−0.144	0.154	−0.149	0.064	−0.122	0.132	−0.109	−0.077	−0.102	−0.259
$M_z/\mu_{\rm B}$	−0.086	−0.006	−0.084	−0.006	−0.065	0.002	−0.040	−0.025	−0.026	−0.054
U'/eV	2		3		4		5			
	$\boldsymbol{R}_{\rm in}$	$\boldsymbol{R}_{\rm out}$	$\boldsymbol{R}_{\rm in}$	$\boldsymbol{R}_{\rm out}$	$\boldsymbol{R}_{\rm in}$	$\boldsymbol{R}_{\rm out}$	$\boldsymbol{R}_{\rm in}$	$\boldsymbol{R}_{\rm out}$		
$M_x/\mu_{\rm B}$	0.000	0.000	0.000	0.000	0.000	0.000	0.000	0.000		
$M_y/\mu_{\rm B}$	−0.108	−0.235	−0.099	−0.076	−0.071	−0.082	−0.049	−0.052		
$M_z/\mu_{\rm B}$	−0.031	−0.040	−0.035	−0.022	−0.026	−0.011	−0.017	−0.002		

We report the magnetization and AFM vectors of Cr with variation of U' in Table 4 and Fig. 2 respectively. As shown in Fig. 2, an anomaly is found at the same U' value of 1.3 eV. In Table 4, Cr_1 and Cr_2 have the same magnetization in the y and z directions showing that the magnetization of these two ions are deviating symmetrically from the original x direction due to the DMI. It is shown that the denser grid tends to give a slightly larger magnetization composition. It is worthwhile mentioning that the different grid schemes provide the same tendency and critical value

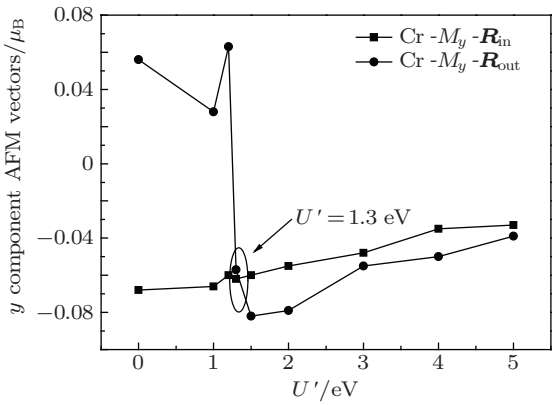


Fig. 2. The y component of AFM vectors of Cr with respect to U'.

prohibiting magnetization reversal. Hereby we use the denser one to investigate the magnetic and electronic properties in the following part. As U' is passing through the critical value, the y component magnetization is decreased significantly in comparison to that in z direction. The critical value prohibiting DMI in $BiFeO_3$ and Bi_2FeMnO_6 is 2.9 eV and 2.7 eV, while that in $BiCrO_3$ is merely 1.3 eV. The Hamiltonian of $BiCrO_3$ can be written as

$$H_{\rm BiCrO_3} = -2 \sum_{\langle {\rm Cr}_i, {\rm Cr}_j \rangle} \boldsymbol{J}_{{\rm Cr}_i,{\rm Cr}_j} \boldsymbol{S}_{{\rm Cr}_i} \cdot \boldsymbol{S}_{{\rm Cr}_j} + \sum_{\langle {\rm Cr}_i, {\rm Cr}_j \rangle} \boldsymbol{D}_{{\rm Cr}_i,{\rm Cr}_j} \cdot \boldsymbol{S}_{{\rm Cr}_i} \times \boldsymbol{S}_{{\rm Cr}_j}. \quad (2)$$

The first term is attributed to the symmetric superexchange, and the second term is the antisymmetric DMI contribution which only occurs when the inversion symmetry of the cations is broken. The constant $\boldsymbol{D}$ is related to the AFD displacement ($\boldsymbol{R}_{\rm in}$ and $\boldsymbol{R}_{\rm out}$) and like a 'DMI constant' which is associated with the magnitude of the DMI. It can be written in the second order perturbation as

$$\boldsymbol{D}^{(2)}_{{\rm Cr}_1,{\rm Cr}_2} = (4{\rm i}/U)[b_{nn'}({\rm Cr}_1 - {\rm Cr}_2) C_{n'n}({\rm Cr}_2 - {\rm Cr}_1) - C_{nn'}({\rm Cr}_1 - {\rm Cr}_2) b_{n'n}({\rm Cr}_2 - {\rm Cr}_2)], \quad (3)$$

It can be seen that the DMI constant is inversely proportional to the on-site Coulomb interaction. Moreover, the DMI constant is also determined by the spin moment of the neighboring magnetic ions. The Cr–Cr antisymmetric interaction where the interacting spin moment are $(3/2)S$–$(3/2)S$ is weaker than the Fe–Mn antisymmetric interaction where the interacting spin moment are $(5/2)S$–$(4/2)S$ and the latter is weaker than that for $BiFeO_3$ where interacting spin moment are $(5/2)S$–$(5/2)S$. This explains why the critical U' in $BiCrO_3$ is the minimum value while that in $BiFeO_3$ is the maximum one.

Table 4. The magnetization for Cr_1 and Cr_2 per unit cell with respect to different values of U'. Cr_1 and Cr_2 are two neighboring chromium ions along the [1 1 1] direction in a one unit cell.

	U'/eV	0		1		1.2		1.3		1.5	
		$\boldsymbol{R}_{\rm in}$	$\boldsymbol{R}_{\rm out}$	$\boldsymbol{R}_{\rm in}$	$\boldsymbol{R}_{\rm out}$	$\boldsymbol{R}_{\rm in}$	$\boldsymbol{R}_{\rm out}$	$\boldsymbol{R}_{\rm in}$	$\boldsymbol{R}_{\rm out}$	$\boldsymbol{R}_{\rm in}$	$\boldsymbol{R}_{\rm out}$
Cr_1	$M_x/\mu_{\rm B}$	2.349	2.492	2.519	2.608	2.544	2.627	2.636	2.556	2.579	2.653
	$M_y/\mu_{\rm B}$	−0.068	0.056	−0.066	0.028	−0.060	0.063	−0.062	−0.057	−0.060	−0.082
	$M_z/\mu_{\rm B}$	−0.030	−0.002	−0.026	−0.002	−0.023	0.001	−0.014	−0.014	−0.014	−0.018
Cr_2	$M_x/\mu_{\rm B}$	−2.349	−2.492	−2.519	−2.608	−2.544	−2.627	−2.636	−2.556	−2.579	−2.653
	$M_y/\mu_{\rm B}$	−0.068	0.056	−0.066	0.028	−0.060	0.063	−0.062	−0.057	−0.060	−0.082
	$M_z/\mu_{\rm B}$	−0.030	−0.002	−0.026	−0.002	−0.023	0.001	−0.014	−0.014	−0.014	−0.018
	U'/eV	2		3		4		5			
		$\boldsymbol{R}_{\rm in}$	$\boldsymbol{R}_{\rm out}$	$\boldsymbol{R}_{\rm in}$	$\boldsymbol{R}_{\rm out}$	$\boldsymbol{R}_{\rm in}$	$\boldsymbol{R}_{\rm out}$	$\boldsymbol{R}_{\rm in}$	$\boldsymbol{R}_{\rm out}$		
Cr_1	$M_x/\mu_{\rm B}$	2.630	2.693	2.716	2.763	2.787	2.824	2.852	2.880		
	$M_y/\mu_{\rm B}$	−0.055	−0.079	−0.048	−0.055	−0.035	−0.050	−0.033	−0.039		
	$M_z/\mu_{\rm B}$	−0.012	−0.016	−0.009	−0.013	−0.005	−0.006	−0.010	−0.001		
Cr_2	$M_x/\mu_{\rm B}$	−2.630	−2.693	−2.716	−2.763	−2.787	−2.824	−2.852	−2.880		
	$M_y/\mu_{\rm B}$	−0.055	−0.079	−0.048	−0.055	−0.035	−0.050	−0.033	−0.039		
	$M_z/\mu_{\rm B}$	−0.012	−0.016	−0.009	−0.013	−0.005	−0.006	−0.010	−0.001		

We further investigate the exchange integrals in $\boldsymbol{R}_{\rm in}$ and $\boldsymbol{R}_{\rm out}$ as U' is changed from 0 eV to 5 eV. The spin exchange parameters have been handled by considering the Heisenberg model,

$$\Delta E = -1/2 \sum_{i,j} J_{i,j} \boldsymbol{S}_i \cdot \boldsymbol{S}_j. \tag{4}$$

The total energy involving the spin exchange interaction can be written as

$$E_{\rm FM} = E_{\rm t} - Z_{\rm Cr} J S^2, \tag{5}$$

for FM spin configuration. Where $E_{\rm t}$ is the total energy without the spin, $Z_{\rm Cr}$ is the number of nearest neighboring Cr ions, and J is the exchange integral. While the AFM total energy reads

$$E_{\rm AFM} = E_{\rm t} + Z_{\rm Cr} J S^2. \tag{6}$$

The total energy to $\boldsymbol{R}_{\rm in}$ and $\boldsymbol{R}_{\rm out}$ in FM and AFM spins as well as the exchange integrals are presented in Figs. 3 and 4, respectively. From Fig. 3, it can be seen that the total energy is increasing monotonically with as U' increases. The inward AFD state exhibits a much favorable energy state compared with the outward AFD state. Hereby there exists a small energy barrier between these two rotational states. An anomaly can be found at around 3 eV for the inward state FM spin configuration. The same phenomenon can be observed in the relationship between the exchange parameter and U' as shown in Fig. 4. The spin configuration to $\boldsymbol{R}_{\rm in}$ is changed to FM order at 3 eV indicating that the AFM exchange interaction is precluded. As we have expected, $\boldsymbol{R}_{\rm in}$ exhibits a much higher exchange integral than $\boldsymbol{R}_{\rm out}$, confirming the favorable state possessed in the energy graph. J decreases as U' increases, indicating that the spin interaction is reduced with a higher effective Hubbard parameter. The reduced spin interaction further lowers the DMI. Hereby there are two side-effects when U' is increasing, one is the direct reduction of the DMI, the other is a reduced J leading to a smaller DMI. Also we provide the magnetic moment for the FM spin configuration in Fig. 5. $\boldsymbol{R}_{\rm in}$ state exhibits a relatively lower magnetic moment compared with the

$\boldsymbol{R}_{\rm out}$ state. It is worthwhile pointing out that there is an anomaly for the inward state at 1.3 eV where the critical value prohibiting the DMI exists. The magnetic moment for the $\boldsymbol{R}_{\rm in}$ state becomes larger than that for the $\boldsymbol{R}_{\rm out}$ state as U' is approaching 5 eV.

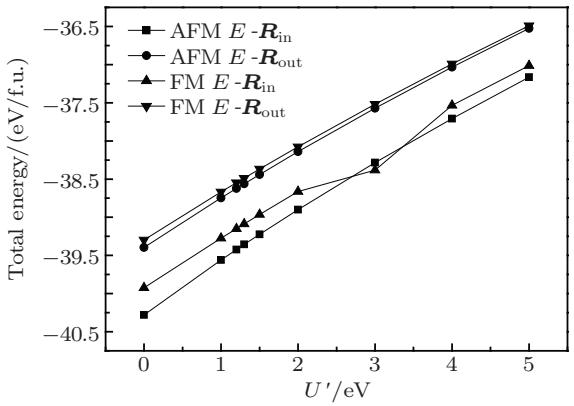


Fig. 3. The total energy per f.u. for the FM and AFM structure in the opposite AFD states as functions of U'.

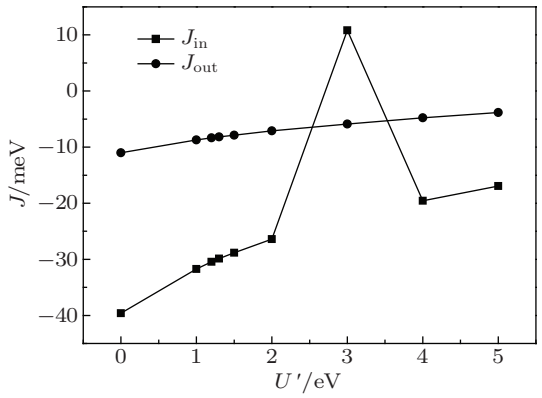


Fig. 4. The exchange integrals for $\boldsymbol{R}_{\rm in}$ and $\boldsymbol{R}_{\rm out}$ as functions of U'.

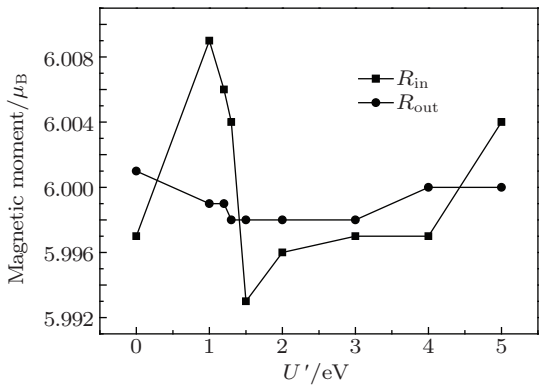


Fig. 5. The FM magnetization as a function of U'.

In order to discover the role of DMI on neighboring Cr ions, we report the total density of states (DOS) and the orbital resolved density of states (ODOS) of Cr to $\boldsymbol{R}_{\rm in}$ and $\boldsymbol{R}_{\rm out}$ states as U' is equal to 0 eV and 5 eV in Figs. 6 and 7, respectively. In the total DOS graph, one can see that the inward state exhibits a metallic behavior without applying the effective Hubbard parameter while the outward state opens a narrow band gap of 0.32 eV due to the specific crystalline field. With the application of U', the finite density of states in the vicinity of the Fermi level have been pushed away to form a band gap of 0.54 eV and 0.92 eV for $\boldsymbol{R}_{\rm in}$ and $\boldsymbol{R}_{\rm out}$ states, respectively. Moreover the large amount of states in the vicinity of the Fermi energy are mainly originating from the Cr–O hybridization characteristics. These states have been pushed away from the Fermi level due to considering the on-site Coulomb interaction on the chromium 3d states. In order to elucidate the role of e_g–e_g states interaction, we report the ODOS of Cr for the corresponding states as shown in Fig. 7. In the perovskite crystalline field Cr-3d states are splitting into doubly degenerate e_g and triply degenerate t_{2g} states. e_g state is composed by $d_{z^2-r^2}$ and $d_{x^2-y^2}$ orbitals, while t_{2g} is composed by d_{xy}, d_{yz}, and d_{xz} orbitals. One can see that the $d_{z^2-r^2}$ orbital is splitting from the e_g states for $\boldsymbol{R}_{\rm in}$ and $\boldsymbol{R}_{\rm out}$ and positions at different energy regions corresponding to different spin polarized states. Through this orbital the neighboring e_g states of Cr-3d can interact with each other in a specific crystalline structure as the cations space inversion symmetry is broken which are exactly the conditions for the DMI to arise. This confirms the conclusion we have drawn for other perovskite magnetoelectrics where the charge hybridization and redistribution between transition metal ions and thus the DMI are realized mainly by the e_g–e_g states interaction. With the application of U' the doubly degenerate e_g states are pushed and positioned at different energy regions to decrease the DMI effect. This forms the microsopic mechanism between DMI and the on-site Coulomb interaction. The different spin polarized states of the $d_{z^2-r^2}$ orbital under opposite AFD distortions permit the opposite rotation of the net magnetization and thus the magnetization reversal mediated by the lattice structure. Moreover the d_{yz} and d_{xz} orbitals are also slightly split from the triply degenerate states. This suggests that the orbitals with a z component are involved in the electronic hybridization and the DMI. The magnetic ions are arranged in a z direction and thus the electronic hybridization and correlation preferentially occurred through orbitals in this direction.

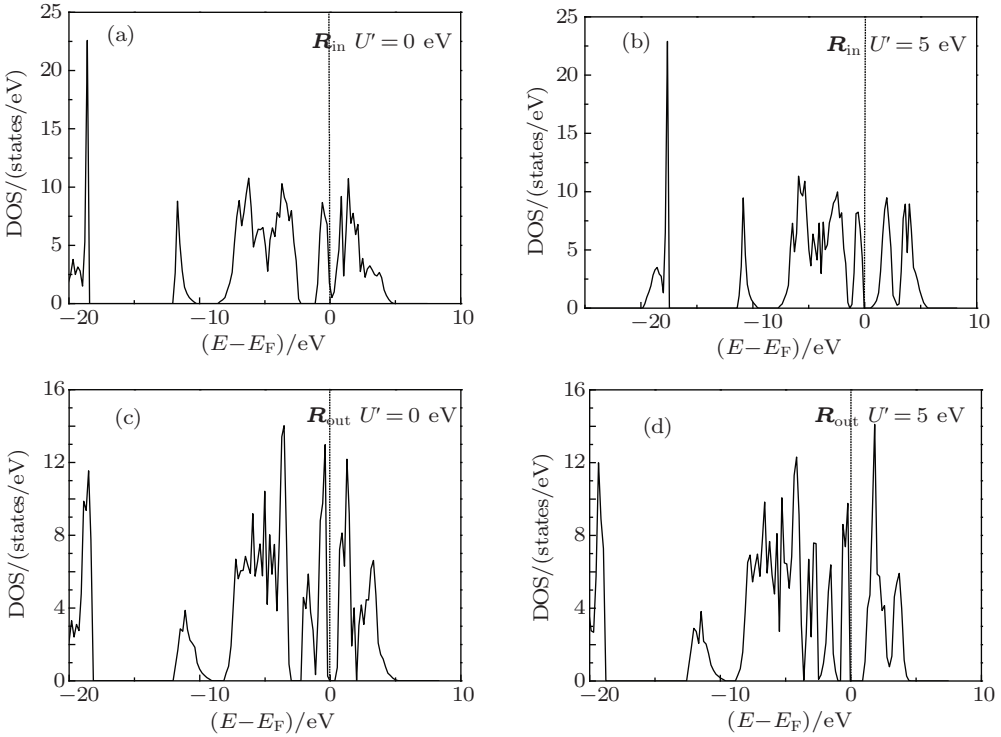


Fig. 6. The total DOS for $\boldsymbol{R}_{\rm in}$ and $\boldsymbol{R}_{\rm out}$ with U'=5 eV and without applying U'. Panels (a), (b), (c), and (d) show the total DOS of inward state with $U'=0$ eV and $U'=5$ eV, the total DOS of outward state with $U'=0$ eV and $U'=5$ eV, respectively. The Fermi level is set to zero.

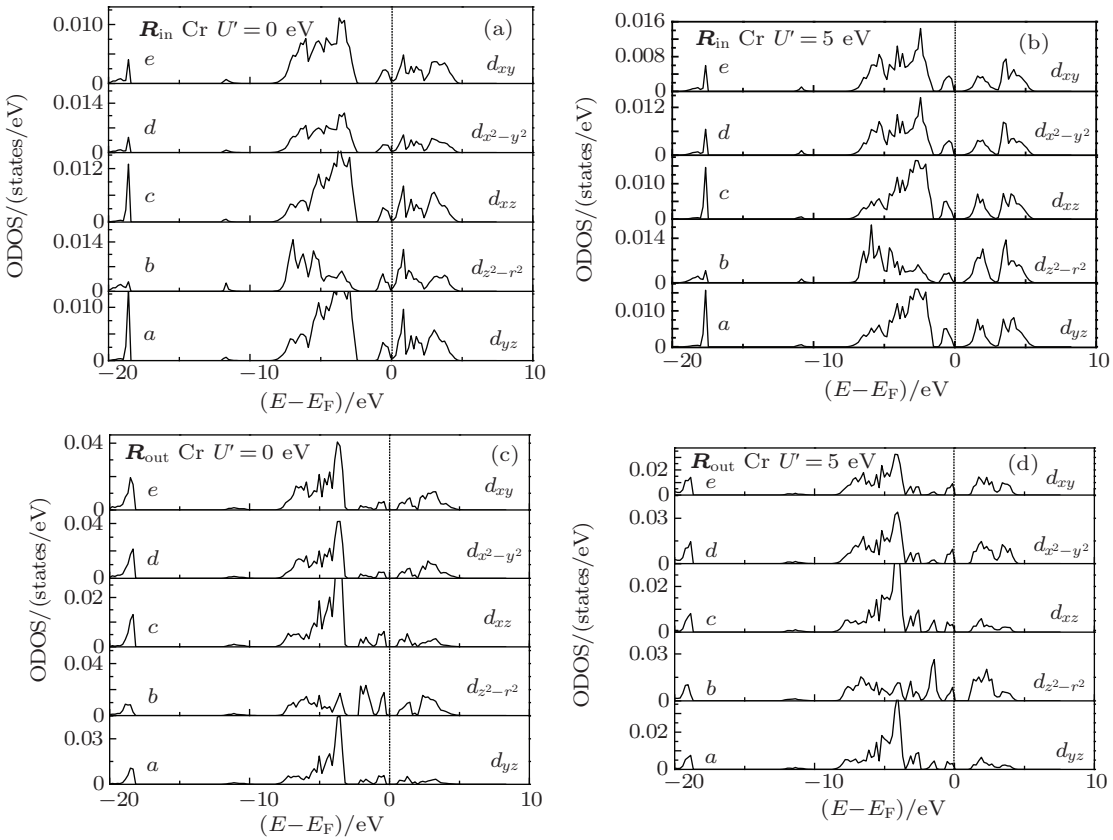


Fig. 7. The ODOS of Cr for $\boldsymbol{R}_{\rm in}$ and $\boldsymbol{R}_{\rm out}$ with $U'=5$ eV and without applying U. Panels (a), (b), (c), and (d) show the ODOS for Cr inward state with $U'=0$ eV and $U'=5$ eV, outward state with $U'=0$ eV and $U'=5$ eV, respectively. Curves a, b, c, d, and e are ODOS for Cr d_{yz}, $d_{z^2-r^2}$, d_{xz}, $d_{x^2-y^2}$, and d_{xy} orbitals, respectively. The Fermi level is set to zero.

4. Conclusion

Ab initio calculations show that the coupling between AFD distortions and magnetization in perovskite $BiCrO_3$ prohibits magnetization rotation, as an effective Hubbard parameter, U', is larger than 1.3 eV. Anomalies in AFM vectors and FM magnetic moments varying with U' are found at the critical value of U'. This coupling is attributed to the antisymmetric DMI driven by the e_g–e_g states AFM interaction and charge redistribution with respect to different AFD distortions.

References

[1] Schmid H 1994 *Ferroelectrics* **162** 317
[2] Fiebig M 2005 *J. Phys.* D: *Appl. Phys.* **38** R123
[3] Wang J, Neaton J B, Zheng H, Nagarajan V, Ogale S B, Liu B, Viehland D, Vaithyanathan V, Schlom D G, Waghmare U V, Spaldin N A, Rabe K M, Wuttig M and Ramesh R 2003 *Science* **299** 1719
[4] Moriya T 1960 *Phys. Rev. Lett.* **4** 228
[5] Moriya T 1960 *Phys. Rev.* **120** 91
[6] Ederer C and Spaldin N A 2005 *Phys. Rev.* B **71** 060401
[7] Feng H J and Liu F M 2008 *Chin. Phys. Lett.* **25** 671
[8] Feng H J 2010 *J. Mag. Mag. Mater.* **322** 1765
[9] Feng H J 2010 *J. Mag. Mag. Mater.* **322** 3755
[10] Feng H J 2012 *J. Mag. Mag. Mater.* **324** 178
[11] Baettig P and Spaldin N A 2005 *Appl. Phys. Lett.* **86** 012505
[12] Nechache R, Harnagea C, Pignolet A, Normandin F, Veres T, Carignan L and Menard D 2006 *Appl. Phys. Lett.* **89** 102902
[13] Baettig P, Ederer C and Spaldin N A 2005 *Phys. Rev.* B **72** 214105
[14] The ABINIT code is a common project of the Universite Catholique de Louvain, Corning, Inc., and other contributors (URL http://www.abinit.org)
[15] Gonze X, Beuken J M, Caracas R, Detraux F, Fuchs M, Rignanes G M, Jollet F, Torrent M, Roy A, Mikami M, Ghosez P, Raty J Y and Alan D C 2002 *Comput. Mater. Sci.* **25** 478
[16] Blochl P E 1994 *Phys. Rev.* B **50** 17953
[17] Kresse G and Joubert D 1999 *Phys. Rev.* B **59** 1758
[18] Anisimov V I, Zaane J and Andersen O K 1991 *Phys. Rev.* B **44** 943
[19] Anisimov V I, Solovyev I V and Korotin M A 1993 *Phys. Rev.* B **48** 16929
[20] Feng H J and Liu F M 2009 *Chin. Phys.* B **18** 1574
[21] Feng H J and Liu F M 2008 *Chin. Phys.* B **17** 1874
[22] Feng H J and Liu F M 2009 *Chin. Phys.* B **18** 2481
[23] Feng H J and Liu F M 2009 *Chin. Phys.* B **18** 2487